Dalton Transactions

ROYAL SOCIETY OF CHEMISTRY

PAPER

View Article Online
View Journal | View Issue

Cite this: *Dalton Trans.*, 2025, **54**, 14150

Electrocatalytic water oxidation with bioinspired cubane-type Co^{II} complexes

Roberto Favela-Mendoza,[a] Elizabeth Rul-Ramírez,[a] Ana Cristina García-Alvarez,[a] Eduardo Sánchez-Lara,[a] Stefani Gamboa-Ramírez,[b] Marcos Flores-Álamo,[c] Sylvain Bertaina,[d] Maylis Orio,[b] Isabel Guerra-Tschuschke[e] and Ivan Castillo *[a]

Synthesis, characterization, and electrocatalytic water oxidation studies of the cubane-type complexes $[(\mu^3\text{-}\mathbf{L^1O})CoCl(MeOH)]_4$ (**1**) and $[(\mu^3\text{-}\mathbf{L^2O})CoCl(MeOH)]_4$ (**2**) are herein reported. Cubanes **1** and **2** were obtained in high yields under mild conditions by self-assembly of the ligands $\mathbf{L^1OH}$ = 1-*H*-2-benzimidazolylmethanol and $\mathbf{L^2OH}$ = 1-methyl-2-benzimidazolylmethanol with $CoCl_2{\cdot}6H_2O$ in basic methanolic solution. Both compounds feature a cubane-type structure in which the central $\{Co_4O_4\}$ units are built by four Co^{II} centers coordinated by alkoxide-bridged oxygen and nitrogen atoms from the deprotonated $\mathbf{L^nOH}$ ligands and stabilized by MeOH molecules and chloride ions. Magnetic studies allowed the determination of g = 2.42 and g = 2.57 values for **1** and **2**, respectively. At low temperatures, **1** shows antiferromagnetic behavior, while **2** shows ferromagnetic coupling. DFT analyses support the antiferromagnetic behavior of **1**. Unfortunately, the same method was not effective at explaining the ferromagnetic character of **2**. Such inconsistency was explained through an exhaustive ac-susceptibility study by considering the single molecular magnet (SMM) behavior of **2**. Cyclic voltammetry of **1** and **2** in phosphate buffer solution (pH = 7.4) displayed catalytic currents at 1.65 and 1.68 V *vs.* Standard Hydrogen Electrode (SHE), corresponding to water oxidation, with TOF values of 1.04 and 1.99 s^{-1}, overpotentials of 710 and 680 mV, faradaic efficiencies of 88% and 90%, and TON values of 2.8 and 3.5 for **1** and **2**, respectively. Electrochemical Quartz Microbalance (EQCM) analysis showed the robustness of **1** and **2** since only around 0.05% of their mass was deposited on the electrode surface. Subsequent SEM-EDX microanalysis demonstrated that although **1** converts to CoO_x during electrolysis, it also changes into an undetermined form of the original catalyst, containing C, O, and Co. In the case of **2**, analysis of the electrode after WOC did not allow the detection of Co, C, or O, establishing **2** as a more stable catalyst than **1**.

Received 28th April 2025,
Accepted 7th July 2025

DOI: 10.1039/d5dt01000d

rsc.li/dalton

1. Introduction

There is an urgent need to develop viable alternatives to fossil fuels.[1] However, renewable energy technologies remain unaffordable and insufficient on a global scale. Emulating nature to harness the sun's energy appears to be the ideal solution, but artificial photosynthesis is still a developing field. Nonetheless, addressing the multielectron reactions involved in photosynthesis through electrocatalysis is crucial in that direction,[2,3] mainly since electrocatalytic processes usually occur at room temperature and pressure. In the long run, solar-powered galvanostatic reactions may ideally replace the need for fossil fuels. In this context, water splitting constitutes one of the most promising alternatives to this end.[4] During this process, water is converted into dioxygen, four protons and four electrons, according to eqn (1):

$$2H_2O \rightarrow O_2 + 4H^+ + 4e^- \quad E^\circ = 1.23\ \text{V}\ \textit{vs.}\ \text{SHE} \qquad (1)$$

The main obstacle is the sluggishness of the anodic reaction due to kinetics involving four protons and four electrons, thus resulting in a high overpotential for the electrochemical oxidation of water. The archetypal ruthenium blue dimer was the first homogeneous electrocatalyst employed successfully in this process.[5] After its discovery, iridium analogs were developed with similar results, with the main disadvantage of their prohibitively high cost. This is the main incentive to search and design a new generation of catalysts based on the abun-

[a]*Instituto de Química, Universidad Nacional Autónoma de México, Circuito Interior, CU, Ciudad de México, 04510, Mexico. E-mail: joseivan@unam.mx*
[b]*Aix Marseille Université, CNRS, Centrale Med, FSCM, Marseille, France*
[c]*Facultad de Química, Universidad Nacional Autónoma de México, Circuito Exterior, CU, Ciudad de México, 04510 Mexico*
[d]*Aix-Marseille Université, CNRS, Université de Toulon, IM2NP, Marseille, France*
[e]*Centro de Instrumentación Científica, Unidad de Microscopia Electrónica de Barrido de Presion Variable, Universidad de Granada, Avda. Prof. Juan Osorio s/n, 18071 Granada, Spain*

dant first-row transition metals capable of efficiently performing the water oxidation reaction. The challenge involves the ease of synthesis and systems with low overpotentials that do not require drastic conditions that may be energetically and environmentally taxing.[6–9]

In the case of cobalt complexes, initial attempts to explore water oxidation involved mononuclear systems coordinated with nitrogen-based ligands. Among these, neutral pentadentate pyridine-derived ligands (PY5),[10,11] tetra-amide macrocyclic ligands (TAML),[12,13] porphyrins,[14,15] and corroles have been employed.[16,17] The above compounds split water successfully without decomposition to cobalt oxides of the general formula CoO_x, with turnover numbers (TON) between 50 and 130 and turnover frequencies (TOF) in the range of one order of magnitude. In all cases, either neutral or basic pH conditions were used in buffered solutions.

Usually, the overpotential values (η) of these systems are about 300–550 mV. An alternative to improve catalytic efficiency relies on high-nuclearity complexes so that the charge buildup may delocalize between two or more metal centers in the high-valent species crucial to oxidize water. The best example of multimetallic cooperative effects is the Oxygen Evolving Complex (OEC) of Photosystem II (PSII), which contains the Mn_4CaO_5 cluster (TOF = 400 s^{-1} and η < 300 mV).[8] Inspired by PSII, the design of polynuclear complexes based on first-row transition metals to mimic the catalytic activity of PSII has grown dramatically. Manganese polymetallic complexes were naturally among the first tested; a 12-nuclear manganese compound reported by Maayan and coworkers[18] displayed good electrocatalytic activity for water oxidation at pH = 6, with TOF = 22 s^{-1} and η = 74 mV. Iron is another versatile metal employed in water splitting and an attractive option as the most abundant transition metal. In 2016, a pentanuclear iron compound[19] was reported with reasonable performance at pH = 5 and a remarkable TOF = 1900 s^{-1}, but a high overpotential at η = 889 mV. In the case of cobalt, Dismukes *et al.* reported in 2011 the first cobalt cubane-type complex that showed activity for water oxidation catalysis (WOC), with TON and TOF values of 40 ± 2 and 0.02 s^{-1}, respectively.[20]

Analogous complexes of the latter system were synthesized by Berardi *et al.* In this case, *para*-substituted pyridine ligands were introduced into the Co_4O_4 unit, improving photoinduced electron transfer.[21] TOF values for these cubane-type complexes lie between 510 and 550 s^{-1}. More recently, Nguyen and coworkers reported mechanistic studies of a related cobalt cubane,[22] evidencing that mixed $Co^{III}_3Co^{IV}$ species afford dioxygen quantitatively. These insights illustrate the principles behind designing robust molecular scaffolds to stabilize high oxidation states while simultaneously exploiting metal–metal cooperativity. In this context, we focused on cubane-type complexes $[(\mu_3\text{-}\mathbf{L^1O})CoCl(MeOH)]_4$ (**1**) and $[(\mu_3\text{-}\mathbf{L^2O})CoCl(MeOH)]_4$ (**2**) ($\mathbf{L^1OH}$ = 1-*H*-2-benzimidazolylmethanol and $\mathbf{L^2OH}$ = 1-methyl-2-benzimidazolylmethanol), based on the self-assembly observed for such ligands and Ni^{II} that affords the corresponding Ni_4O_4 cubanes under mild conditions.[23] In contrast, the corresponding Br-containing analogs $[(\mu_3\text{-}\mathbf{L^nO})CoBr(ROH)]_4$ were previously obtained under harsh conditions, but their electrochemical and electrocatalytic properties were not reported.[24] Thus, we present the facile synthesis, solid-state and electrochemical characterization, and WOC assessment of **1** and **2**.

2. Results and discussion

2.1 Synthesis and structural description

Ligands $\mathbf{L^1OH}$ and $\mathbf{L^2OH}$ react with $CoCl_2{\cdot}6H_2O$ and two equivalents of triethylamine in methanol to afford **1** and **2** in high yields as purple and dark pink powders through a self-assembly process depicted in Scheme 1. Compounds **1** and **2** were subsequently crystallized by slow vapor diffusion of 1,1,2,2-tetrachloroethane into methanolic solutions. Pink needle- and prism-type crystals of **1** and **2** were thus obtained after several days. Single crystal X-ray diffraction reveals that **1** crystallizes in the triclinic space group $P\bar{1}$. As shown in Fig. 1, the compound has a central $[Co_4(\mu_3\text{-}OR)_4]^{4+}$ core consisting of four alkoxo-bridged cobalt ions in a distorted cubane-type structure, with the oxygen atoms from the deprotonated $\mathbf{L^1O^-}$ ligands and the Co^{II} ions in alternate corners of the cube.

Each octahedral Co^{II} ion has the same coordination environment, with four oxygen atoms, three of which are μ^3-bridges and one terminal MeOH. The octahedral positions are completed by a potentially labile chloride ligand and a benzimidazole N-donor from $\mathbf{L^1O^-}$. Thus, each ligand acts in $\mu^3{:}\eta^3{:}\eta^1$ fashion.[25–27] Two lattice MeOH molecules placed in general positions complete the asymmetric unit of **1**. As is evident from the crystallographic data, distortion of the cubane $\{Co_4O_4\}$ is caused by the differences in the Co–O distances and the variation between the Co–O–Co and O–Co–O bond angles relative to an ideal structure with T_d symmetry, see Table 1.

In this context, the Co–O and Co–N bond lengths are in the range of 2.046(4)–2.170(4) Å and 2.070(5)–2.126(5) Å, respectively, which are comparable to those reported for similar cubane-type clusters assembled with heterocyclic aromatic systems.[24,28] On the other hand, the smallest angle within $\{Co_4O_4\}$ is 78.94(15)° for O(3)–Co(4)–O(1), while the largest one is 99.63(16)° for Co(1)–O(3)–Co(4). The distorted tetrahedron defined by the Co^{II} centers has four different Co···Co distances in the range of 3.148(1)–3.256(1) Å, indicating that **1** has a low symmetry cubane core, resulting in six different $\{Co_2O_2\}$ faces. This complex is isostructural with the tetranuclear Ni^{II} cubane

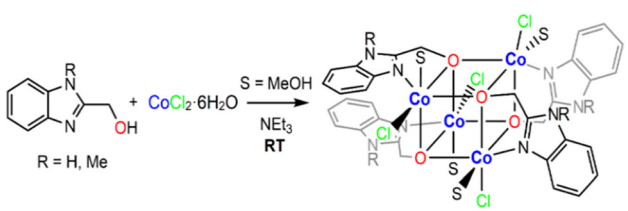

Scheme 1 Self-assembly of $[(\mu^3\text{-}L^nO)CoCl(S)]_4$.

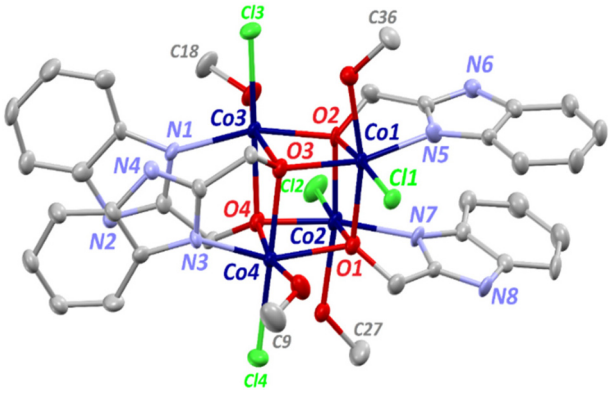

Fig. 1 ORTEP view of **1** with atom-labeling scheme. Displacement ellipsoids at a 60% probability level; H atoms and lattice MeOH molecules are omitted for clarity.

Table 1 Selected bond lengths and angles for **1** and **2**

	1	**2**
Co–Cl (Å)	2.3770(16)–2.4822(15)	2.3737(15)
Co–O (Å)	2.046(4)–2.158(4)	2.078(4)–2.155(4)
Co–N (Å)	2.070(5)–2.126(5)	2.091(5)
Co···Co (Å)	3.148(1)–3.256(1)	3.169(1)–3.257(1)
$Co–O_{MeOH}$ (Å)	2.113(4)–2.170(4)	2.155(4)
O–Co–O (°)	78.94(15)–82.12(16)	80.15(15)–81.39(15)
O–Co–N (°)	77.47(16)–105.48(17)	77.94(17)–99.51(17)
Co–O–Co (°)	95.74(15)–99.75(17)	97.81(15)–99.51(15)

reported recently by our group as a robust electrocatalyst for water oxidation (CSD Refcode: OYOLOG).[23] Thus, comparing the catalytic performance of these structurally related complexes should provide insight into the effect of transition metal substitution in these clusters.

Complex **1** is stabilized by intra- and intermolecular contacts (Fig. 2). The chloride ligands are involved in intramolecular H-bonds with the coordinated MeOH molecules on four faces of the cubane *via* O–H···Cl contacts with distances in the range of 2.20(5)–2.30(6) Å, and D–H···A angles ranging

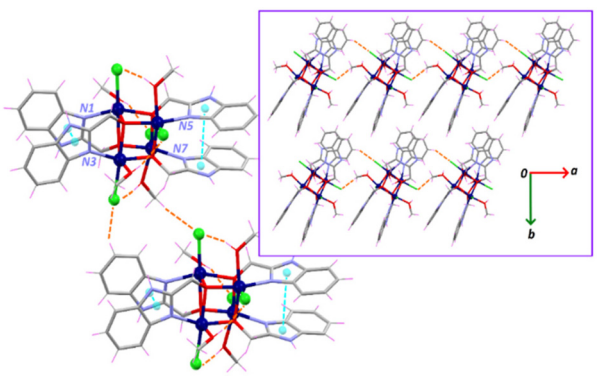

Fig. 2 Extended crystal structure of **1** with π–π contacts, intra- and intermolecular C–H···Cl hydrogen bonds represented by dotted cyan and orange lines, respectively. The inset displays the packing, highlighting the C–H···Cl interactions between adjacent molecules.

from 149(3) to 160(7)°. The benzimidazole groups of the $\mathbf{L^1O^-}$ ligands extend outward from opposite faces of the cubane in a parallel arrangement that favors intramolecular π–π interactions between the imidazole moieties, characterized by centroid-to-centroid distances of 3.43(4) and 3.48(5) Å between the N1/N3 and the N5/N7 rings, respectively (Fig. 2).[29,30] Such interactions may confer stability to **1** and direct the self-assembly of $\{M_4O_4\}$ clusters.[31,32] In addition, a lattice MeOH molecule forms an intermolecular H-bond with one of the chloride ligands with an O(9)–H(9)···Cl(2) distance of 2.32(4) Å. In a supramolecular context, the molecules are packed within the crystal perpendicular to the crystallographic *c*-axis and interact with each other *via* short intermolecular C–H···Cl contacts (Fig. 2, inset).

As detailed in the Experimental section, compound **2** was obtained similarly to **1**, except that the *N*-methylated $\mathbf{L^2OH}$ replaces $\mathbf{L^1OH}$. The complex crystallizes in the tetragonal system of the $P\bar{4}2_1c$ space group with a quarter of $[(\mu_3\text{-}\mathbf{L^2O})CoCl(MeOH)]_4$ in the asymmetric unit (Fig. S1), so that **2** is characterized by S_4 molecular symmetry. As in the previous structure, the four cobalt(II) octahedral ions are located at alternate corners of a distorted cubane in which the μ^3-bridging O-atoms of the four deprotonated $\mathbf{L^2OH}$ ligands occupy the remaining four vertices. The Co^{II} centers have the same octahedral coordination pattern as in **1**, with Co–O distances in the range of 2.078(4)–2.155(4) Å and a single bond length of 2.091(5) Å for the four Co–N bonds. The Co···Co distances in the central $\{Co_4O_4\}$ core are in the range of 3.169(1)–3.257(1) Å.

An overlay of both solid-state structures using OLEX2 software reveals that the central $[Co_4(\mu_3\text{-}OR)_4]^{4+}$ units do not show significant structural differences[33] (Fig. S2). This is the case for both the organic and chloride ligands, which are almost aligned. However, changes in the rotational orientation of the $-CH_3$ groups of the coordinated methanol molecules are observed; these can be explained by packing effects and the presence of the *N*-Me substituent on the benzimidazole backbone, causing the methoxy groups to move away. In addition, the $-CH_3$ groups from the coordinated MeOH molecules of **1** are involved in weak C–H···O and C–H···Cl intermolecular hydrogen bonds. In contrast, no intermolecular interactions for the coordinated MeOH molecules are observed in **2**. The same behavior is observed with isostructural cubane-type complexes with MeOH as coordinating molecules.[24] It is worth noting that the Co···Co distances in both $\{Co_4O_4\}$ central cores are comparable to the Mn···Mn distances observed for the natural $[Mn_4CaO_5]$ cubane found in PSII, which fall in the range of 2.8–3.0 Å.[34,35] While the Mn and Ca ions coordinate water molecules potentially involved in the oxygen evolution reaction (OER), in complexes **1** and **2**, the MeOH molecules and chloride ligands can be replaced by substrate water molecules *via* ligand exchange. Our group has already studied the feasibility of this process in related Ni cubanes by experimental and theoretical methods.[23]

In **2**, the organic moieties are also paired face-to-face on the opposite sides of the cube, allowing the MeOH molecules and chloride atoms to coordinate in a plane perpendicular to the

L^2O^- ligands. Therefore, the coordinated methanol molecules of **2** are also involved in intramolecular interactions with the Cl^- ions, characterized by an O–H···Cl distance of 2.23(16) Å and a D–H···A angle of 165.7(3)°. The imidazole moieties establish symmetrically equivalent π stacking interactions with a centroid-to-centroid separation of 3.41(5) Å. Intermolecular π–π interactions between the six-member aromatic groups are not observed in either of the two structures. The packing of **2** is stabilized by short intermolecular C–H···Cl interactions, as observed in the inset of Fig. S3. In related work, Zeng and co-workers reported an isostructural complex in 2017 (CSD refcode: NENYIR), where the $[Co(OR)]_4$ cubane consisted of octahedral Co(II) centers chelated by the alkoxide oxygen and imidazole N atom from the same L^2O^- ligand but coordinated by bromides instead of chlorides.[24] However, the complex was studied purely from a magnetic perspective without exploring its electrochemical properties.

2.2 Mass spectrometry

For the complexes with the formula $[(\mu^3\text{-}L^nO)CoBr(ROH)]_4$, structural rearrangements were observed in MeOH under mass spectrometry conditions involving the reorganization of the cubane structure to low-nuclearity species such as Co_1, Co_2 or Co_3, but also oligomerization of these to produce higher nuclearity fragments.[24] Interestingly, ESI-MS and FAB^+ spectra of **1** and **2** confirmed this type of behavior *via* low-intensity peaks at *m*/*z* 558.5 (calc. 559.3) and 601.0 (calc. 601.4) corresponding to $[(\mu^3\text{-}L^1O)_3Co_2]^+$ and $[(\mu^3\text{-}L^2O)_3Co_2]^+$, respectively (Fig. S4 and S5). Thus, the cubane system is stable at room temperature and pressure but can undergo transformations under harsher conditions, like those present in the ionization chamber.[36,37] Nonetheless, for **1** the most intense peak at *m*/*z* 930.2 (calc. 930.7) corresponds to the cubane structure $[(\mu^3\text{-}L^1O)_4Co_4Cl_3]^+$ following the loss of all MeOH molecules and a chloride ion. For **2**, the species $[(\mu^3\text{-}L^2O)_4Co_4Cl_3]^+$ was observed with low intensity at *m*/*z* 987 (calc. 986.8). Since the catalytic activity of **1** and **2** was examined in phosphate buffer solutions (KPi, pH = 7.4), their stability was analyzed after one week in KPi solutions. MALDI-TOF MS of **1** displayed a low-intensity peak at *m*/*z* 875.0 (calc. 875.4) corresponding to the $[(\mu^3\text{-}L^1O)_4Co_4(OH)_3]^+$ fragment, resulting from the loss of MeOH and the substitution of the Cl^- ions by hydroxy groups. In the case of **2**, the analogous fragment was not observed, but the base peak at *m*/*z* 584.9 (calc. 585.1) is consistent with the peculiar arrangement $[(\mu^2\text{-}L^2O)_2Co_2(\mu^2\text{-}OH)(MeOH)_4]^+$ (Fig. S6 and S7).

2.3 Magnetic properties

The magnetic susceptibilities of **1** and **2** were measured from 300 K to 1.8 K with a field of 1 T. The χ^{-1} *vs.* *T* curves presented in Fig. 3 show two different temperature behaviors. We fitted the experimental data using the Curie–Weiss mean field susceptibility, $\chi_m = \frac{C}{T-\theta}$, and we obtained Curie constants, *C*, of 10.98 $cm^3\ mol^{-1}$ K and 12.39 $cm^3\ mol^{-1}$ K for **1** and **2**, respectively, which are indicative of a non-negligible orbital contribution from the Co(II) centers. Using the Curie formula in CGS units, *i.e.* $C = \frac{1}{8} \times g^2 \times S(S+1) \times n$, and considering $n = 4$ for a high spin Co^{II} cubane, we obtain $g = 2.42$ and 2.57 for **1** and **2**, respectively. These two values are comparable to previously reported data for the bromo analogues at room temperature.[23] The main difference between **1** and **2** appears to be low-temperature behavior. Indeed, the mean-field Curie–Weiss constant *Q* is negative for **1** ($Q = -8.16$ K), indicative of antiferromagnetic coupling, while for **2** we obtain $Q = +22.51$ K, a value suggesting a dominant ferromagnetic coupling.

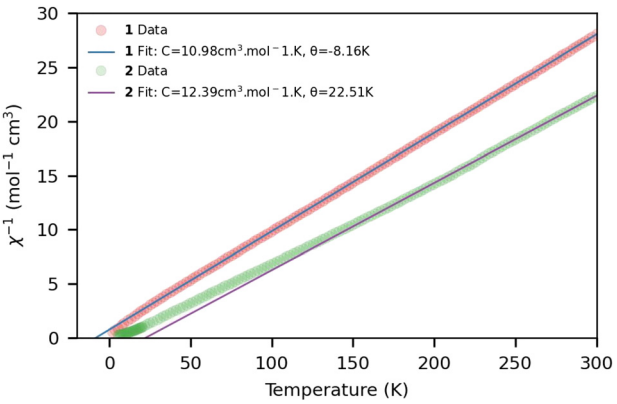

Fig. 3 $\chi_M T$ *vs.* *T* plot for **1** and **2** (*H* = 1000 Oe) showing the best-fitting in the 2–300 K range.

Density Functional Theory (DFT) calculations using the Broken-Symmetry (BS) framework[38–40] were performed to get further insight into the magnetic behavior of **1** and **2**. Following the same approach we employed in previous works,[23,41] the systems were considered as magnetically coupled and treated as *N* spin sites interacting through $N(N-1)/2$ exchange couplings J_{ij}, using the isotropic Heisenberg–Dirac–van Vleck (HDvV) Hamiltonian, *i.e.* $H = -2 \times \sum_{i<j} J_{ij} S_i S_j$.[42–45]

BS-DFT calculations determined six possible pairwise exchange coupling constants for the four magnetically coupled Co^{II} ions in **1** and **2**. We computed the eight possible spin configurations for the two complexes: a $S = 6$ high spin (HS) configuration, four $M_S = 3$ BS solutions, and three $M_S = 0$ BS solutions (Fig. S8). The energy of each spin configuration was expressed as a linear combination of the local spin of each cobalt center and the individual exchange coupling constant; we generated a series of eight equations, which is solved using singular value decomposition (SVD). Using this methodology, the following J_{ij} values were obtained: $J_{12} = +2.35$, $J_{13} = +2.33$, $J_{14} = -2.85$, $J_{23} = -2.84$, $J_{24} = +2.34$ and $J_{34} = +2.32$ cm^{-1} for **1** and $J_{12} = +1.26$, $J_{13} = +1.26$, $J_{14} = -1.24$, $J_{23} = -1.22$, $J_{24} = +1.18$ and $J_{34} = +1.18$ cm^{-1} for **2**. Direct diagonalization of the HDvV Hamiltonian provided the magnetic sublevel spectra for both complexes (Tables S1 and S2), showing that **1** and **2** feature a singlet ground spin state ($S = 0$).

The computed exchange coupling constants in **1** thus support an antiferromagnetic interaction between the cobalt centers and are in good agreement with the experimental data. The simulated magnetic susceptibility curve ($\chi_m \cdot T$ *vs.* *T*) for **1**

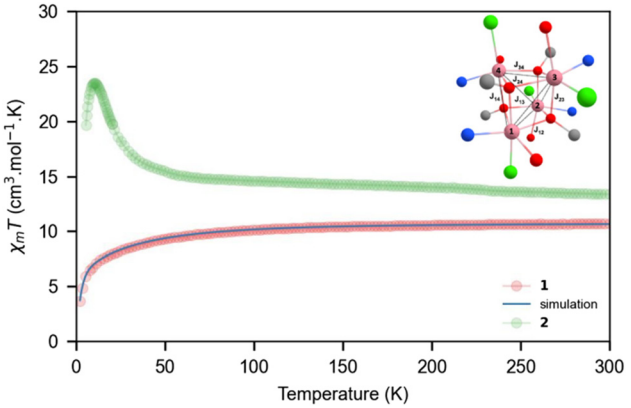

Fig. 4 Temperature dependence of the product $\chi_m \cdot T$ of **1** and **2**. The red and green circles correspond to the experimental data for the two complexes. The solid blue line was calculated using the theoretical values J_{12} = +2.35, J_{13} = +2.33, J_{14} = −2.85, J_{23} = −2.84, J_{24} = +2.34, J_{34} = +2.32 cm^{-1}, and D = 33 cm^{-1}. Inset: Schematic view of relevant exchange pathways in **1**.

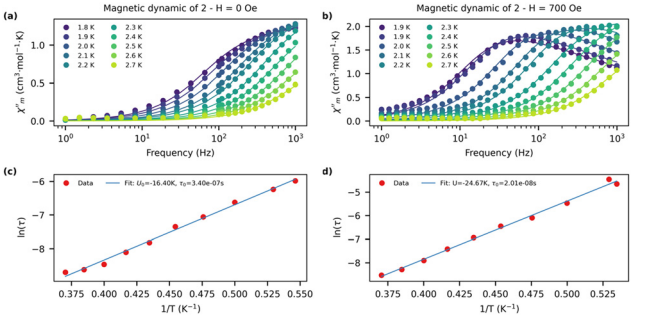

Fig. 5 Frequency dependence of the imaginary part of the ac-susceptibility of **2** recorded as a function of the temperature from 1.8 to 2.7 K and under a bias field of 0 Oe (a) and 700 Oe (b). Arrhenius law presented as logarithmic dependence of τ as function of 1/T for 0 Oe (c) and 700 Oe (d). Symbols give extracted times, and lines give least-squares fits.

using the computed set of J_{ij} is shown in Fig. 4 (blue curve) together with the experimental data (red circles) and highlights the good correlation between theory and experiment. However, our calculations fail to reproduce the ferromagnetic interaction experimentally observed for **2**. We tentatively assign this discrepancy to a probable single molecular magnet (SMM) behavior of **2**, preventing computations from providing meaningful predictions of the exchange interactions.

To investigate the SMM behavior of **2**, we conducted a detailed ac-susceptibility study. We first measured the in-phase χ' and out-phase χ'' susceptibilities at T = 1.8 K across a frequency range spanning from 0.1 to 1450 Hz and applied various external dc-fields spanning from 0 to 3000 Oe. This process aimed to determine the optimal external magnetic field to minimize quantum tunneling. We then measured the ac-susceptibility as a function of both frequency and temperature, ranging from 1.8 to 4 K for H_0 = 0 and 700 Oe (Tables S3, S4 and Fig. S9–S12).

The evolution of χ'' as a function of frequency was subsequently fitted using the imaginary part of the Cole–Cole equation to extract the relaxation time t (Fig. 5). The temperature-dependent relaxation times were then analyzed under the assumption of a thermally activated process, following the Arrhenius law: $\tau_0 = \tau_0 \times e^{U_{eff}/k_B T}$. We obtained U_{eff} = −16.47 K and $\tau_0 = 3.06 \times 10^{-7}$ s for H_0 = 0 Oe, and U_{eff} = −24.67 K and $\tau_0 = 2.0 \times 10^{-8}$ s for H_0 = 700 Oe. The resulting parameters for **2** compare well with previously reported values for other characterized cubane compounds and support the suggested SMM behavior.

2.4. Electrochemical analyses

The cubane-type complexes **1** and **2** were analyzed by cyclic voltammetry (CV) from 0 to 1.8 V *vs.* the Standard Hydrogen Electrode (SHE) under an Ar atmosphere. The experiments revealed an irreversible anodic peak E_{ap} = 1.68 for **1** and E_{ap} = 1.65 V for **2**, Fig. S13. CV of fresh 0.01 M KPi solution shows no faradaic current in the working potential range. The observed $E_{ap1} > E_{ap2}$ can be explained in terms of inductive effects from the ligand to the Co^{II} center; in complex **2** *N*-methyl groups on the benzimidazole moiety are stronger electron donors than hydrogen atoms, making the metal centers in **2** slightly more electron-rich than those in **1**. Current measurements at different sweep rates (plot of i_{pa} *vs.* $\nu^{1/2}$) demonstrate that the current is limited by diffusion of the analyte to the electrode surface, with diffusion coefficients D = 1.83×10^{-4} and 2.41×10^{-5} cm^2 s^{-1} for **1** and **2**, respectively (Fig. 6 and S15).

When the current is normalized ($i/\nu^{1/2}$), it is evident that the process is catalytic since i_{cat} decreases when the sweep rate increases (Fig. S16). The overpotential (η) value for **1** and **2** is 710 and 680 mV, respectively, and it was determined using the equation $\eta = |E_{H_2O/O_2} - E_{cat/2}|$ and calculating the water oxidation potential with the relation $E_{H_2O/O_2}[V\ vs.\ NHE] = 1.23 - 0.059 \times pH$, and $E_{cat/2}$ is the potential value at half the intensity of the catalytic current.[46] To dismiss the participation of free Co^{II} ions in the electrocatalytic water oxidation process, bulk electrolysis experiments of $CoCl_2 \cdot 6H_2O$ in KPi were carried out. The results show that the charge generated employing the cobalt complexes is considerably higher than that with $CoCl_2 \cdot 6H_2O$ at pH = 7.4 (Fig. S14). Indirect proof of dioxygen formation was obtained through CV identification of the wave assigned to its reduction to superoxide (E_p = −0.66 V, Fig. S17). Thus, bulk electrolysis (BE) with a 1 mM solution of **2** was set at 1.68 V for 15 minutes to produce dioxygen, and immediately, a second BE was set at −1.1 V to produce superoxide for further 15 min. The charge produced in this experiment was compared to that generated during BE at −1.1 V of a fresh solution of **2**. As expected, the charge was considerably higher when the cobalt complex carried out WOC before superoxide detection (Fig. S18). Direct dioxygen quantification was carried out through BE experiments at 1.71 and 1.68 V for **1** and **2** (0.1 mM), respectively. After 1 h, the production of O_2 was determined with a fluorescent probe, resulting in values of 9.0

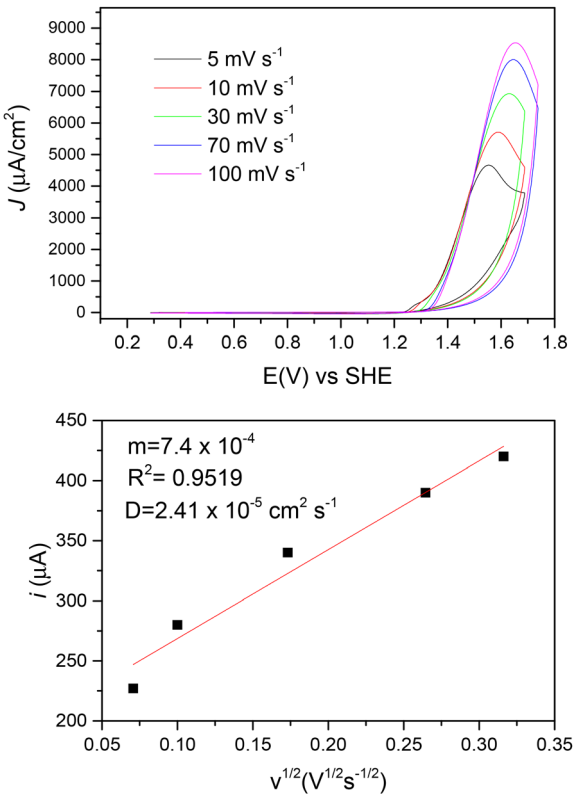

Fig. 6 Top: CV of **1** at different scan rates. Bottom: plot i_{pa} *vs.* $\nu^{1/2}$. Conditions: [**1**] = 1 mM in KPi 0.1 M, pH = 7.4; glassy carbon working electrode, Ag/AgCl reference electrode, Pt counter electrode.

and 11.4 ppm for **1** and **2**, corresponding to 88% and 90% faradaic efficiencies (Fig. S19), and modest TON values of 2.8 and 3.5.

A critical aspect of WOC is catalyst stability during the demanding redox process. This was addressed initially through analysis of the UV-vis spectra of **1** and **2** before and after electrolysis, with only minor changes observed (Fig. S20). Subsequently, Electrode Quartz Crystal Microbalance (EQCM) experiments were used to quantify the material deposited on the electrode surface. During the experiment, 60 cycles of CV of **1** were carried out, and at the same time, the EQCM measured the change in the frequency of the quartz disc covered with a gold monolayer as the working electrode. A frequency change of 4000 Hz was registered at the end of the experiment, taking 0 Hz as the initial frequency value. Considering that a change in 2.25 Hz corresponds to 3.35 ng of mass deposited on the electrode, 5.95 μg of material derived from **1** remained at the electrode after WOC. This amount corresponds to 0.05% of the total mass of the catalyst in solution, indicating that **1** and **2** are robust under the catalytic conditions (Fig. S21). Additionally, rinse tests were carried out on **1** and **2**. The working electrode used in these experiments was then tested in fresh KPi solutions, and no considerable catalytic current was observed during CV. These results confirm the predominant homogeneous nature of the WOC, establishing **1** and **2** as robust catalysts that do not give rise to cobalt oxide deposits (Fig. S22).

Catalytic currents of complexes **1** and **2** were analyzed at different concentrations, and a linear correlation was found for each one, demonstrating that the rate law is first-order for both catalysts (Fig. S23). Analysis of CV data collected in D_2O-based buffer affords inverse isotope effect values of 0.79 and 0.68 for **1** and **2**, respectively (Fig. S24, Tables S8 and S9). These may correspond to an equilibrium isotope effect (EIE), rather than a kinetic one, consistent with O–O bond formation at adjacent cobalt-oxyl sites as the rate-limiting step;[47] this can be envisioned at two cobalt sites on one of the faces in cubane, in an I2M-type mechanism. This would also result in a positive shift of the oxidation potential, which in our case was determined at 55 and 80 mV.[47] Based on data analysis and using the foot-of-the-wave (FOWA) methodology developed by Savéant and Costentin,[48] the calculated TOF values for **1** and **2** are 1.04 and 1.99 s^{-1}, respectively (Fig. S25). It is worth mentioning that the direct comparison of these TOF values with other cobalt systems reported in the literature can be misleading due to the diverse experimental conditions employed to carry out WOC (aqueous or non-aqueous media, type of buffer, pH values, and the catalyst oxidation method: chemical, electrochemical or photoinduced).

Comparison of the WOC activity of **1** and **2** relative to other Co cubanes is difficult since the conditions employed vary significantly. For example, $Co_4^{III}O_4(OAc)_4(py)_4$ (py = pyridine) was tested under standard photocatalytic conditions with $Ru^{II}(bpy)_3^{2+}$ (bpy = bipyridine) and the sacrificial electron acceptor $Na_2S_2O_8$.[20] Related $Cu_4^{III}O_4(OAc)_4(pyX)_4$ systems (X = Me, *t*Bu, OMe, Br, COOMe, and CN), were developed to explore the electronic effects of *para*-substitution in the pyridine ligands within the Co_4O_4 unit; a TON value of 140 for all complexes under similar photocatalytic conditions, but TOF values were not reported.[21] A cubane-type Co(II) complex $[Co_4^{II}(hmp)_4(\mu\text{-}OAc)_2(\mu_2\text{-}OAc)_2(H_2O)_2]$ featuring 2-hydroxymethylpyridine (hmp) was also used for photoinduced WOC, achieving the best result at pH = 9 in borate buffer solution, with TOF = 7 s^{-1} and TON = 28.[49] So far, cobalt cubane-type complexes have been considered relatively stable species during WOC. Nonetheless, further examination of $Co_4O_4(OAc)_4(py)_4$ and its analogue $Co_4O_4(OAc)_4(pyCOOMe)_4$ by Differential Electrochemical Mass Spectrometry (DEMS) indicated that catalytic activity was not inherent to the molecular $Co_4^{III}O_4$ unit, but instead to a Co^{II} impurity.[50] Since then, there has been a debate about whether cobalt oxides or molecular cobalt complexes act as true catalysts. The debate continued through the analysis of the complex Co(HL) (HL = *N*,*N*-bis(2,2′-bipyrid-6-yl)amine) by electrochemical quartz crystal microbalance (EQCM) and X-ray photoelectron spectroscopy.[51] These demonstrated that although the molecular Co(HL) interacts with the electrode surface, this does not necessarily imply that it transforms into cobalt oxides; our results support this latter observation. Finally, $Co_4^{III}O_4(OAc)_4(py)_4$ was characterized electrochemically, allowing the determination of an overpotential of 728 mV at pH 12, and TOF = 0.2 s^{-1}.[22] In contrast, **1** and **2**

have slightly lower overpotentials at neutral pH. The information from the above discussion is summarized in Table 2.

Moreover, when the water splitting process is electrocatalytic, there is an inherent problem related to the TOF calculation due to the need for an accurate normalization of the Electrochemical Surface Area (ECSA) of the electrode, which is never equal to the geometrical area. Currently, there is a debate regarding this topic given that, to date, there are only a few methods to normalize ECSA.[52] In this sense, **1** and **2** show relatively good activity, considering that until 2022,[53] the collected information covered 34 cobalt complexes, from which only for 22 complexes the TOF values were reported. The lowest and highest TOF values within these are 6.2×10^{-6} and 1400 s^{-1}, respectively. From the total, eight complexes (36%) possess TOF values under 1 s^{-1}; nine (41%) between 1 and 10 s^{-1}; four (18%) between 10 and 100 s^{-1}; and only one complex shows a TOF = 1400 s^{-1}. According to this information, most cobalt catalysts employed in WOC possess activity between 1 and 10 s^{-1}. **1** (1.04 s^{-1}) and **2** (1.99 s^{-1}) belong to this category with relatively good activity, considering only their TOF values (Table S10). Nevertheless, it is hard to compare them directly since most reports omit overpotential values.

2.5. SEM EDX analyses

The gold electrodes used in ECQM experiments were interrogated by scanning electron microscopy (SEM) to analyze the material deposited after 60 scans of cyclic voltammetry. The SEM image of **1** at 1 mm reveals needle-like and amorphous materials (Fig. S25). Energy Dispersive X-ray (EDX) microanalysis further uncovered that these regions are predominantly carbon-based (Fig. S26). Nevertheless, images at 25 μm showed zones with different topologies; one of these (zone 12, see Fig. S27) was observed at 1 μm and 100 nm and exhibited hexagonal deposits (Fig. 7), with EDX elemental maps confirming the presence of Au, C, O, Co, and Cl (Fig. S28), as well as three distinct phases: Co–C, C–O, and Co–O (Fig. 8) which indicates that carbon is bound with cobalt and oxygen in the same regions of the deposited material. Complex **1** may transform into different species during electrolysis but was not completely degraded to CoO_x.

Note that nitrogen was not detected in any EDX spectrum; therefore, the Co–N phase does not appreciably form. Cobalt oxides were also detected by observing the Co–O phase, even though the area is considerably smaller than that of the Co–C and C–O phases. These observations are consistent with the previously reported partial decomposition of cobalt-based catalysts during WOC in phosphate buffer solutions to cobalt oxide.[54] However, this happens to a small extent in the case of **1**. Despite the reported evidence of deposition of cobalt complexes that afford heterogeneous catalysts on electrode surfaces, in our case, cyclic voltammetry experiments of **1** and **2** indicate a catalyst deactivation process, with the subtle difference that it does not lead to a significant amount of cobalt oxide formation. If that were the case, an increase in the catalytic current would be expected since cobalt oxides are known to catalyze the water-splitting process. Instead, the catalytic current decreases after several cycles. A rinse test of the working electrodes in fresh buffer solutions provided further evidence of the homogeneous nature of the catalytic activity of **1**.

The electrode used in WOC with **2** revealed polygonal structures (Fig. 8). Interestingly, EDS analysis showed that this material is exclusively carbon (Fig. S29). EDS maps of carbon and gold demonstrate the absence of Co, O, Cl, or other elements (Fig. S30), leading us to conclude that electrolysis of **2** results in less deposition of cobalt than **1** under the conditions employed. Moreover, a rinse test of the electrode in a fresh buffer solution showed the absence of catalytic current, supporting the above observations.

Table 2 TOF and TON values of some Co_4O_4 systems used as WOC

Complex used as WOC	TOF (s^{-1})	TON	Ref.
1[a]	1.04	2.8	This work
2[a]	1.99	3.5	This work
$Co_4O_4(OAc)_4(py)_4$[b]	0.20	40	20 and 22
$Co_4O_4(OAc)_4(pyX)_4$[c] (X = Me, *t*Bu, OMe, Br, COOMe, CN)	–	140	21
$[Co^{II}_4(hmp)_4(\mu\text{-}OAc)_2(\mu_2\text{-}OAc)_2(H_2O)_2]$[d]	7	28	49

[a] KPi buffer 0.1 M, pH = 7.4, electrocatalytic. [b] Borate buffer 50 mM, pH = 9. [c] Borate buffer 10 mM, pH = 8. [d] Sodium phosphate buffer 0.1 M, pH = 8.

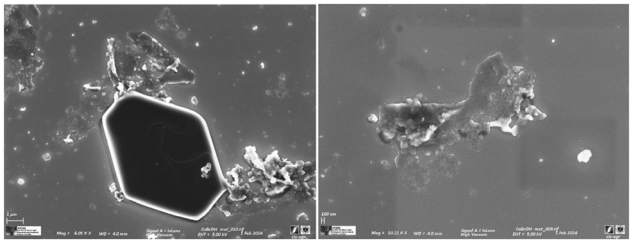

Fig. 7 SEM images of the ECQM electrode (quartz with a gold monolayer) used in water oxidation catalysis using **1** in 0.01 M phosphate buffer.

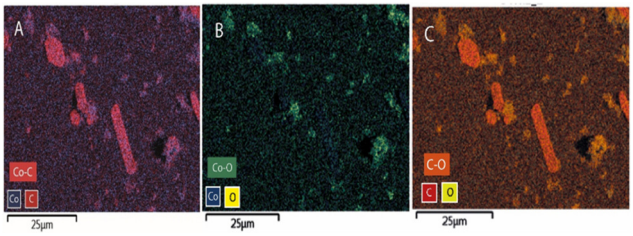

Fig. 8 EDS elemental maps of different phases: (A) Co–C, (B) Co–O, and (C) C–O.

3. Conclusions

The cobalt cubane-type complexes **1** and **2** were successfully synthesized under mild conditions and demonstrated efficient

catalytic activity in water oxidation, with turnover frequencies of 1.04 and 1.99 s^{-1} and overpotentials of 710 and 680 mV, respectively. Electrochemical studies confirmed that WOC is predominantly homogeneous, as evidenced by the absence of catalytic currents after electrode rinse tests. Stability assessments indicated that both complexes exhibit high robustness, with minimal structural transformation during catalysis. While **1** undergoes partial conversion into cobalt oxide and other species, complex **2** remains structurally intact, highlighting its superior stability. Developing such cobalt-based catalysts is crucial for advancing sustainable energy solutions, as first-row transition metals offer a viable alternative to the more toxic and scarce precious metals. These findings reinforce the potential of cobalt cubane-type complexes as promising candidates for efficient and durable water oxidation catalysis.

4. Experimental

4.1 Reagents and measurements

All chemicals have the highest commercially available purity and were used as received unless noted otherwise. The ligand 1-methyl-2-benzimidazolemethanol (**L^2OH**) was synthesized according to reported procedures,[55] while **L^1OH** was obtained from commercial suppliers. Elemental analyses were performed with a Thermo Scientific elemental analyzer Flash 2000, at a temperature of 950 °C using an XP6 Mettler Toledo microbalance; methionine from Thermo Scientific with certification number 237031 was used as standard. UV-vis spectra were obtained with an Agilent 8453 spectrometer at room temperature. The electrochemical experiments were carried out in a CH Instruments 1400 potentiostat. A three-cell electrode was employed for Cyclic Voltammetry (CV) and Bulk Electrolysis (BE) experiments, using Ag/AgCl (0.1 M KCl) as RE, vitreous carbon (3 mm diameter) as WE, and Pt wire as CE. An ITO electrode was used for bulk electrolysis. A buffer phosphate KPi 0.1 M at pH 7.4 was chosen as electrolyte and solvent for all electrochemical measurements. Electrode potential values are reported against the SHE (Standard Hydrogen Electrode). ^{1}H NMR spectra were recorded on a Bruker Avance 300 MHz spectrometer. EPR spectra were obtained with an Electronic Paramagnetic Resonance Spectrometer Jeol, JES-TE300. Dioxygen quantification was carried out through bulk electrolyses at 1.71 and 1.68 V for **1** and **2** for 1 h under the conditions described above, with an Ocean Optics NeoFox fluorescent probe. Reported values are the average of two measurements.

4.2 Synthesis of complexes

$[(\mu^3\text{-}L^1O)CoCl(MeOH)]_4$ (1). 1-*H*-2-Benzimidazolmethanol (**L^1**, 0.06 g, 0.40 mmol) and $CoCl_2{\cdot}6H_2O$ (0.11 g, 0.40 mmol) were stirred at room temperature for 45 min in methanol, in the presence of two equivalents of triethylamine (93 μL, 0.80 mmol). A violet solid deposited over this time, and it was filtered, washed with diethyl ether (3 × 2 mL), and finally dried under vacuum. M.p. (dec) 195–197 °C; yield 95%. ESI-MS *m*/*z* 930.2 $[Co_4(L^1O)_4Cl_3]^+$. Combustion analysis calc. for $C_{36}H_{44}Cl_4N_8Co_4O_8$ C, 39.51; H, 4.05; N, 10.24%. Found C, 39.22.; H, 3.80; N, 10.31%. IR (KBr) 3057 cm^{-1} (C_{Ar}–H); 2977 cm^{-1} (C–H); 2924 cm^{-1} (C–H); 1570 cm^{-1} (C═N); 1454 cm^{-1}; 1396 cm^{-1}; 1277 cm^{-1}; 837 cm^{-1}. UV-vis (MeOH): 211 nm (ε = 17 180 M^{-1} cm^{-1}), 243 (6370), 273 (8940), 281 (9160), 296 (1580), 340 (430), 670 (24).

$[(\mu^3\text{-}L^2O)CoCl(MeOH)]_4$ (2). 1-Methyl-2-benzimidazolmethanol (**L^2**, 0.06 g, 37 mmol) and $CoCl_2{\cdot}6H_2O$ (0.1 g, 0.37 mmol) were stirred at room temperature for 45 min in methanol, in the presence of two equivalents of triethylamine (85 μL, 0.74 mmol). The dark pink precipitate that formed was filtered, washed with diethyl ether (3 × 2 mL), and dried under vacuum. M.p. (dec.) 220–222 °C, yield 86%. ESI-MS *m*/*z* 987 $[Co_4(L^2O)_4Cl_3]^+$ (Fig. S2). Combustion analysis calc. for $C_{40}H_{52}Cl_4N_8Co_4O_8$ C, 41.76; H, 4.56; N, 9.74%. Found C, 41.46; H, 4.25; N, 9.80%. IR (KBr) 3057 cm^{-1} (C_{Ar}–H); 2977 cm^{-1} (C–H); 2924 cm^{-1} (C–H); 1570 cm^{-1} (C═N); 1454 cm^{-1}; 1396 cm^{-1}; 1277 cm^{-1}; 837 cm^{-1}. UV-vis (MeOH): 211 nm (ε = 17 180 M^{-1} cm^{-1}), 243 (6370), 273 (8940), 281 (9160), 296 (1580), 340 (430), 670 (24).

4.3 X-Ray crystallography

Suitable single crystals of **1** and **2** were mounted on a glass fiber and crystallographic data were collected with an Oxford Diffraction Gemini "A" diffractometer with a CCD area detector using graphite monochromated $\lambda_{CuK\alpha}$ = 1.54184 Å for **1** and $\lambda_{MoK\alpha}$ = 0.71073 Å for **2** at 130 K. Unit cell parameters were determined with a set of three runs of 15 frames (1° in ω). The double-pass method of scanning was used to exclude any noise. The collected frames were integrated by using an orientation matrix determined from the narrow frame scans. CrysAlisPro and CrysAlisRED software packages[56] were used for data collection and integration. Analysis of the integrated data did not reveal any decay. Collected data were corrected for absorption effects by an analytical numeric absorption correction using a multifaceted crystal model based on expressions of the Laue symmetry with equivalent reflections.[57] Structure solution and refinement were carried out using the SHELXT-2018[58] and SHELXL-2018[59] programs, respectively. WinGX v2020[60] was used to prepare the material for publication. Full-matrix least-squares refinement was done by minimizing $(F_o^2 - F_c^2)^2$. All non-hydrogen atoms were refined anisotropically. H atoms of the methanol (O–H) and amine (N–H) groups were located in the difference map and refined isotropically with U_{iso}(H) of 1.5U_{eq} and 1.2U_{eq} for H–O and N–H, respectively. Hydrogen atoms attached to carbon atoms were placed in geometrically idealized positions and refined as riding on their parent atoms, with C–H = 0.95–0.99 Å with U_{iso}(H) = 1.2U_{eq}(C) for methylene and aromatic groups, and U_{iso}(H) = 1.5U_{eq}(C) for methyl groups. Crystal data and experimental details of the structure determination are listed in Table 3. Crystallographic data have been deposited at the Cambridge Crystallographic Data Center as ESI CCDC: 2171997–2171998.

Table 3 Crystallographic data and structural refinement details for **1** and **2**

Compound	**1**	**2**
Chemical formula	$C_{38}H_{51}Cl_4Co_4N_8O_{10}$	$C_{10}H_{13}ClCoN_2O_2$
FW	1157.39	287.60
Temperature	130(2) K	130(2) K
Wavelength	1.54184 Å	0.71073 Å
Crystal system	Triclinic	Tetragonal
Space group	$P\bar{1}$	$P\bar{4}2_1c$
Unit cell dimensions	a = 10.7873(6) Å	a = 10.9927(4) Å
	b = 14.0178(5) Å	b = 10.9927(4) Å
	c = 16.3701(8) Å	c = 19.6735(19) Å
	α= 86.686(3)°	α = 90.00°
	β = 72.875(5)°	β= 90.00°
	γ= 86.271(4)°	γ = 90.00°
V (Å^3)	2358.7(2) Å^3	2377.3(3) Å^3
Z	2	8
$D_{calc.}$(mg m^{-3})	1.630	1.607
Absorption coefficient	13.434 mm^{-1}	1.654 mm^{-1}
F(000)	1182	1176
Theta range for data collection	4.157 to 68.245°	3.618 to 29.355°
Reflections collected	20 662	13 714
Independent reflections	8573 [R(int) = 0.1168]	2945 [R(int) = 0.0761]
GOF on F^2	1.009	1.196
Final R index [$I > 2\sigma(I)$]	R_1 = 0.0697, wR_2 = 0.1759	R_1 = 0.0482, wR_2 = 0.1003
R indices (all data)	R_1 = 0.0961, wR_2 = 0.2001	R_1 = 0.0794, wR_2 = 0.1112

4.4 Magnetic measurements

Magnetic susceptibility measurements were performed using an MPMS-XL5 Quantum Design SQUID magnetometer. Direct current (dc) susceptibility measurements were performed at temperatures ranging from 1.8 to 300 K and performed on powder samples of 11.1 mg **1** and 13.3 mg **2**, wrapped in a polypropylene pocket and vacuum sealed to remove oxygen. Alternating current (ac) susceptibility measurements on **2** were performed on a 33.8 mg sample under an oscillating ac field of 2.9 Oe and ac frequencies ranging from 0.1 to 1433 Hz. The magnetic data were corrected for diamagnetic contributions using Pascal's constants.

4.5 Computational methods

All theoretical calculations were based on density functional theory (DFT) and have been performed using the ORCA program package.[61] To facilitate comparisons with experiment, the X-ray structures of the complexes were optimized while constraining the positions of all heavy atoms to their experimentally derived coordinates and only the positions of the hydrogen atoms were relaxed. Geometry optimization was performed for the high-spin (HS) state with the GGA functional BP86[62,63] using the TZVP[64] basis set for all atoms and by taking advantage of the resolution of the identity (RI) approximation in the Split-RI-J variant[65] with the appropriate Coulomb fitting sets.[66] Scalar relativistic effects were included using ZORA[67] with ZORA-def2-TZVP basis sets.[61] Increased integration grids (Grid4 in ORCA convention) and tight SCF convergence criteria were used. Single-point Broken-Symmetry[38,39] DFT calculations were performed with the hybrid functional B3LYP.[68,69] All spin configurations for Broken-Symmetry calculations were generated with the "FlipSpin" feature of ORCA. The diagonalization of the HDvV Hamiltonian leading to the magnetic sublevel spectrum of the tetranuclear species was performed by employing the orca_eca utility of ORCA. The magnetic susceptibility curve was reconstructed using the Easyspin program[70] and the isotropic Heisenberg–Dirac–Van Vleck (HDvV) exchange Hamiltonian.[45–48]

4.6 Scanning electron microscopy (SEM)

Scanning electron microscopy measurements were conducted using a Variable Pressure Scanning Electron Microscope Zeiss SUPRA 40VP coupled with an EDX Oxford Axtec system at the Scientific Instrumentation Center of the Granada University in Spain. The electrodes which contained samples **1** and **2** were covered by a gold monolayer before running experiments to protect them from decomposition by ionization.

Author contributions

The manuscript and the results included were prepared through contributions of all authors. All authors have given approval to the final version of the manuscript.

Conflicts of interest

The authors declare no competing financial interest.

Data availability

The data supporting this article have been included as part of the SI:

additional spectroscopic, computational, crystallographic, and solid-state characterization. See DOI: **https://doi.org/10.1039/d5dt01000d**. Magnetic data are available at Zenodo repository: **https://doi.org/10.5281/zenodo.16948314**.

CCDC 2171997 and 2171998 contain the supplementary crystallographic data for this paper.[71a,b]

Acknowledgements

The authors thank CONAHCyT (Beca 695554, Proyecto A1-S-8286), DGAPA-PAPIIT (IN216823), IR INFRANALYTICS FR2054 and the French National Research Agency (CUBISM, grant no. ANR-18 CE092 0040 01) for financial support. E. S.-L. thanks SECIHTI for the postdoctoral fellowship 554096.

References

1 Y. Zhou, *Energy Rev.*, 2023, **2**, 100026.

2 J. Masa, C. Andronescu and W. Schuhmann, *Angew. Chem., Int. Ed.*, 2020, **59**, 15298–15312.
3 R. I. Walton, Inorganic Materials Chemistry, in *Comprehensive Inorganic Chemistry III*, ed. J. Reedijk and K. R. Poeppelmeier, Elsevier, Amsteram, 2023.
4 H. Yang, X. Han, A. I. Douka, L. Huang, L. Gong, C. Xia, H. S. Park and B. Y. Xia, *Adv. Funct. Mater.*, 2021, **31**, 2007602.
5 S. W. Gersten, G. J. Samuels and T. J. Meyer, *J. Am. Chem. Soc.*, 1982, **104**, 4029–4030.
6 M. Gil-Sepulcre and A. Llobet, *Nat. Catal.*, 2022, **5**, 79–82.
7 L. H. Zhang, S. Mathew, J. Hessels, J. N. H. Reek and F. Yu, *ChemSusChem*, 2021, **14**, 234–250.
8 M. Kondo, H. Tatewaki and S. Masaoka, *Chem. Soc. Rev.*, 2021, **50**, 6790–6831.
9 Q. F. Chen, Y. H. Guo, Y. H. Yu and M. T. Zhang, *Coord. Chem. Rev.*, 2021, **448**, 214164.
10 D. J. Wasylenko, R. D. Palmer, E. Schott and C. P. Berlinguette, *Chem. Commun.*, 2012, **48**, 2107–2109.
11 B. Das, A. Orthaber, S. Ott and A. Thapper, *Chem. Commun.*, 2015, **51**, 13074–13077.
12 D. Das, S. Pattanayak, K. K. Singh, B. Garai and S. Sen Gupta, *Chem. Commun.*, 2016, **52**, 11787–11790.
13 H.-Y. Du, S.-C. Chen, X.-J. Su, L. Jiao and M.-T. Zhang, *J. Am. Chem. Soc.*, 2018, **140**, 1557–1565.
14 T. Nakazono, A. R. Parent and K. Sakai, *Chem. Commun.*, 2013, **49**, 6325–6327.
15 D. Wang and J. T. Groves, *Proc. Natl. Acad. Sci. U. S. A.*, 2013, **110**, 15579–15584.
16 D. K. Dogutan, R. McGuire and D. G. Nocera, *J. Am. Chem. Soc.*, 2011, **133**, 9178–9180.
17 H. Lei, A. Han, F. Li, M. Zhang, Y. Han, P. Du, W. Lai and R. Cao, *Phys. Chem. Chem. Phys.*, 2014, **16**, 1883–1893.
18 T. Ghosh and G. Maayan, *Angew. Chem., Int. Ed.*, 2019, **58**, 2785–2790.
19 M. Okamura, M. Kondo, R. Kuga, Y. Kurashige, T. Yanai, S. Hayami, V. K. K. Praneeth, M. Yoshida, K. Yoneda, S. Kawata and S. A. Masaoka, *Nature*, 2016, **530**, 465–468.
20 N. S. McCool, D. M. Robinson, J. E. Sheats and G. C. Dismukes, *J. Am. Chem. Soc.*, 2011, **133**, 11446–11449.
21 S. Berardi, G. La Ganga, M. Natali, I. Bazzan, F. Puntoriero, A. Sartorel, F. Scandola, S. Campagna and M. Bonchio, *J. Am. Chem. Soc.*, 2012, **134**, 11104–11107.
22 A. I. Nguyen, M. S. Ziegler, P. Oña-Burgos, M. Sturzbecher-Hohne, W. Kim, D. E. Bellone and T. D. Tilley, *J. Am. Chem. Soc.*, 2015, **137**, 12865–12872.
23 A. C. García-Álvarez, S. Gamboa-Ramírez, D. Martínez-Otero, M. Orio and I. Castillo, *Chem. Commun.*, 2021, **57**, 8608–8611.
24 X. F. Ma, Z. Wang, X. L. Chen, M. Kurmoo and M. H. Zeng, *Inorg. Chem.*, 2017, **56**, 15178–15186.
25 S. H. Zhang, L. F. Ma, H. H. Zou, Y. G. Wang, H. Liang and M. H. Zeng, *Dalton Trans.*, 2011, **40**, 11402–11409.
26 M. Zhang, T. Yang, Z. Wang, X. F. Ma, Y. Zhang, S. M. Greer, S. A. Stoian, Z. W. Ouyang, H. Nojiri, M. Kurmoo and M. H. Zeng, *Chem. Sci.*, 2017, **8**, 5356–5361.
27 Y. L. Zhou, M. H. Zeng, X. C. Liu, H. Liang and M. Kurmoo, *Chem. – Eur. J.*, 2011, **17**, 14084–14093.
28 X. Y. Song, Y. H. Xu, L. C. Li, D. Z. Liao and Z. H. Jiang, *Inorg. Chim. Acta*, 2007, **360**, 2039–2044.
29 D. P. Malenov and S. D. Zarić, *Coord. Chem. Rev.*, 2020, **419**, 213338.
30 C. A. Janiak, *J. Chem. Soc., Dalton Trans.*, 2000, 3885–3896.
31 C. Deville, M. Granelli, A. M. Downward, C. Besnard, L. Guenée and A. F. Williams, *Dalton Trans.*, 2014, **43**, 12917–12925.
32 Y. Q. Hu, M. H. Zeng, K. Zhang, S. Hu, F. F. Zhou and M. Kurmoo, *J. Am. Chem. Soc.*, 2013, **135**, 7901–7908.
33 O. V. Dolomanov, L. J. Bourhis, R. J. Gildea, J. A. K. Howard and H. Puschmann, *J. Appl. Crystallogr.*, 2009, **42**, 339–341.
34 Y. Umena, K. Kawakami, J. R. Shen and N. Kamiya, *Nature*, 2011, **473**, 55–60.
35 J. R. Shen, *Annu. Rev. Plant Biol.*, 2015, **66**, 23–48.
36 Q. J. Deng, M. Chen, D. C. Chen and C. A. Chen, *Crystals*, 2019, **9**, 477.
37 W. F. Xie, L. Y. Guo and J. H. Xu, *Eur. J. Inorg. Chem.*, 2016, 3253–3261.
38 L. Noodleman, *J. Chem. Phys.*, 1981, **74**, 5737–5743.
39 L. Noodleman and E. R. Davidson, *Chem. Phys.*, 1986, **109**, 131–143.
40 L. Noodleman and D. A. Case, *Adv. Inorg. Chem.*, 1992, **38**, 423–470.
41 A. Kochem, B. Faure, S. Bertaina, E. Rivière, M. Giorgi, M. Réglier, M. Orio and A. J. Simaan, *Eur. J. Inorg. Chem.*, 2018, 5039–5046.
42 P. A. M. Dirac, *Proc. R. Soc. London, Ser. A*, 1929, **123**, 714–733.
43 W. Heisenberg, *Z. Phys.*, 1926, **38**, 411–426.
44 W. Heisenberg, *Z. Phys.*, 1928, **49**, 619–636.
45 J. H. Van Vleck, *Nature*, 1932, **130**, 490–491.
46 V. Fourmond, P.-A. Jacques, M. Fontecave and V. Artero, *Inorg. Chem.*, 2010, **49**, 10338–10347.
47 C. Pasquini, I. Zaharieva, D. González-Flores, P. Chernev, M. R. Mohammadi, L. Guinodi, R. D. L. Smith and H. Dau, *J. Am. Chem. Soc.*, 2019, **141**, 2938–2948.
48 C. Costentin, S. Drouet, M. Robert and J. M. Savéant, *J. Am. Chem. Soc.*, 2012, **134**, 11235–11242.
49 F. Evangelisti, R. Güttinger, R. Moré, S. Luber and G. R. Patzke, *J. Am. Chem. Soc.*, 2013, **135**, 18734–18737.
50 A. M. Ullman, Y. Liu, M. Huynh, D. K. Bediako, H. Wang, B. L. Anderson, D. C. Powers, J. J. Breen, H. D. Abruña and D. G. Nocera, *J. Am. Chem. Soc.*, 2014, **136**, 17681–17688.
51 D. Den Boer, Q. Siberie, M. A. Siegler, T. H. Ferber, D. C. Moritz, J. P. Hofmann and D. G. H. Hetterscheid, *ACS Catal.*, 2022, **12**, 4597–4607.
52 S. Anantharaj, P. E. Karthik and S. Noda, *Angew. Chem., Int. Ed.*, 2021, **60**, 23051–23067.
53 W. C. Hsu and Y. H. Wang, *ChemSusChem*, 2022, **15**, e202102378.

54 D. den Boer, Q. Siberie, M. A. Siegler, T. H. Ferber, D. C. Moritz, J. P. Hofmann and D. G. H. Hetterscheid, *ACS Catal.*, 2022, **12**, 4597–4607.
55 S. K. Poddar, N. Saqueeb and S. M. Abdur Rahman, *Dhaka Univ. J. Pharm. Sci.*, 2016, **15**, 83–87.
56 *CrysAlis Pro software system*, Oxford Diffraction Ltd, Oxford, UK, 2007.
57 R. C. Clark and J. S. Reid, *Acta Crystallogr., Sect. A:Found. Crystallogr.*, 1995, **51**, 887–897.
58 G. M. Sheldrick, *Acta Crystallogr., Sect. A:Found. Adv.*, 2015, **71**, 3–8.
59 G. M. Sheldrick, *Acta Crystallogr., Sect. C:Struct. Chem.*, 2015, **71**, 3–8.
60 L. J. Farrugia, *J. Appl. Crystallogr.*, 2012, **45**, 849–854.
61 F. Neese, *Wiley Interdiscip. Rev.:Comput. Mol. Sci.*, 2012, **2**, 73–78.
62 J. P. Perdew, *Phys. Rev. B:Condens. Matter Mater. Phys.*, 1986, **33**, 8822.
63 A. D. Becke, *Phys. Rev. A*, 1988, **38**, 3098.
64 A. Schäfer, C. Huber and R. Ahlrichs, *J. Chem. Phys.*, 1994, **100**, 5829–5835.
65 F. Neese, *J. Comput. Chem.*, 2003, **24**, 1740–1747.
66 F. Weigend, *Phys. Chem. Chem. Phys.*, 2006, **8**, 1057–1065.
67 E. van Lenthe, J. G. Snijders and E. J. Baerends, *J. Chem. Phys.*, 1996, **105**, 6505–6516.
68 A. D. Becke, *J. Chem. Phys.*, 1993, **98**, 5648–5652.
69 C. Lee, W. Yang and R. G. Parr, *Phys. Rev. B:Condens. Matter Mater. Phys.*, 1988, **37**, 785.
70 S. Stoll and A. Schweiger, *J. Magn. Reson.*, 2006, **178**, 42–55.
71 (*a*) CCDC 2171997: Experimental Crystal Structure Determination, 2025, DOI: **10.5517/ccdc.csd.cc2bx4fv**; (*b*) CCDC 2171998: Experimental Crystal Structure Determination, 2025, DOI: **10.5517/ccdc.csd.cc2bx4gw**.